ELSEVIER

Journal of Quantitative Spectroscopy & Radiative Transfer 108 (2007) 371–388

Journal of Quantitative Spectroscopy & Radiative Transfer

www.elsevier.com/locate/jqsrt

Measurements of the O_2 *A*- and *B*-bands for determining temperature and pressure profiles from ACE–MAESTRO: Forward model and retrieval algorithm

C.R. Nowlan[a,*], C.T. McElroy[a,b], J.R. Drummond[a,c]

[a]*Department of Physics, University of Toronto, 60 St. George Street, Toronto, Ont., Canada M5S 1A7*
[b]*Environment Canada, 4905 Dufferin Street, Toronto, Ont., Canada M3H 5T4*
[c]*Department of Physics and Atmospheric Science, Dalhousie University, Halifax, NS, Canada B3H 3J5*

Received 3 April 2007; received in revised form 8 June 2007; accepted 11 June 2007

Abstract

The ACE-MAESTRO (Atmospheric Chemistry Experiment–Measurement of Aerosol Extinction in the Stratosphere and Troposphere Retrieved by Occultation) instrument on the SCISAT satellite is able to measure solar occultation absorption in the *A*- and *B*-bands of molecular oxygen with a spectral resolution of 2 nm. Profiles of total atmospheric density are derived by exploiting the constant and known mixing ratio of O_2, and are used to determine profiles of pressure and temperature using hydrostatic balance and the ideal gas law. A highly accurate combined fast-line-by-line and extended correlated-*k* technique is implemented to fast forward model MAESTRO's O_2 absorption measurements, which ensures that errors in pressure and temperature resulting from the forward model approximation are essentially negligible. Estimated errors in pressure and temperature are determined for the *A*-, *B*-, and combined *A*–*B*-band retrievals for a typical retrieval, and demonstrate that pressure profiles should be derivable to within 1% and temperature to within 2 K over most altitudes using a combined *A*–*B* retrieval. The combined retrieval provides an improvement of up to 0.25% in pressure and 0.5 K in temperature over the *A*-band retrieval alone. The *B*-band could also be used alone below about 50 km, where its independent retrieval produces error estimates of 1–1.5% in pressure and 2–3 K in temperature.

Keywords: Remote sounding; Oxygen *A*-band; Oxygen *B*-band; Temperature; Pressure; Solar occultation; MAESTRO

1. Introduction

The Measurement of Aerosol Extinction in the Stratosphere and Troposphere Retrieved by Occultation (MAESTRO) instrument [1] was launched on the Canadian satellite SCISAT on August 12, 2003, as part of the Atmospheric Chemistry Experiment (ACE) [2]. MAESTRO collects solar occultation spectra between 400 and 1010 nm, with a spectral resolution between 1.5 and 2 nm. Three bands of molecular oxygen are observed by MAESTRO in the visible and near-infrared: the strong *A*-band centred at 762 nm, the weaker *B*-band at

*Corresponding author. Tel.: +1 416 971 2363; fax: +1 416 978 8905.
E-mail address: caroline.nowlan@utoronto.ca (C.R. Nowlan).

0022-4073/$ - see front matter © 2007 Elsevier Ltd. All rights reserved.
doi:10.1016/j.jqsrt.2007.06.006

690 nm, and the much weaker γ-band at 630 nm. In this paper, we develop and test a method for determining atmospheric pressure and temperature profiles from MAESTRO's on-orbit observations of solar absorption in the O_2 *A*- and *B*-bands.

MAESTRO's primary data contributions to the ACE mission are measurements of ozone, NO_2, and aerosol extinction. However, pressure and temperature (p–T) profiles are necessary for properly removing the molecular scattering component from spectra (primarily for separation from aerosol extinction), using temperature-dependent cross-sections, determining mixing ratios from constituent number densities, and accurately calculating the path of a refracted solar ray. While p–T profiles are available from other observing systems, including satellites and radiosondes, and forecast and analyses databases, on-orbit p–T measurements from MAESTRO are highly desirable both for reliable constituent retrievals and as another independent data product. Simultaneous measurement of p–T with other constituents ensures geolocated measurements through the entire measurement altitude range with a consistent instrument field of view (FOV). Profiles could also be used as part of a larger data set for examining stratospheric temperature trends, or in polar stratospheric cloud studies.

MAESTRO's p–T accuracy requirements are determined by the desired uncertainty contribution to the ozone and NO_2 mixing ratio profiles. A 1% error contribution to the mixing ratios can be achieved with a 1% uncertainty in density, which implies a 1% uncertainty in pressure or absolute temperature, so that the p–T accuracy requirement for MAESTRO is 1% in pressure and 2–3 K in temperature.

Several space-based missions have exploited the constant vertical mixing ratio of O_2 for remote sounding of the atmosphere. Yamamoto and Wark [3] were the first to suggest using reflected sunlight in the *A*-band to measure air columns for determining cloud-top height. Their work was further developed in several theoretical studies for cloud-top height and pressure retrieval and surface pressure retrieval [4–7]. Several recent satellite-based sensors have carried sensors in the *A*-band for measurements of cloud-top height and surface pressure [8–11]. The planned Orbiting Carbon Observatory (OCO) mission [12] will use the *A*-band to determine O_2 columns for deriving high-accuracy CO_2 mixing ratios.

While the use of the *A*-band for cloud-top remote sounding has been fairly extensive, the use of the *A*- and *B*-bands for pressure and temperature remote sounding has been less common. The limb-scanning High-Resolution Doppler Imager (HRDI) on the Upper Atmosphere Research Satellite (UARS) used *A*-band emission to derive mesospheric and lower thermospheric temperatures [13]. Dayglow emission in the *A*-band has also been used to measure temperatures in the mesosphere by sounding rockets [14,15]. Matsuzaki et al. [16] used solar absorption rocket observations of the rotational profile of the *A*-band to derive atmospheric temperature at a tangent altitude of 21 km.

The retrieval of pressure and temperature profiles from the *A*-band has been attempted with two space-based solar occultation instruments: the Stratospheric Aerosol and Gas Experiment III (SAGE III) and the Improved Limb Atmospheric Sounder (ILAS). The feasibility of using a low-resolution spectrometer for *A*-band p–T solar occultation retrievals was originally demonstrated using simulated measurements for SAGE III, which has a resolution of about 1.4 nm in the *A*-band. These simulated retrievals indicated uncertainties in pressure of 2% and temperature of 2 K should be achievable from 0 to 85 km, with uncertainty contributions from measurement noise, aerosol clearing, O_2 spectroscopic database and ozone cross-sections uncertainties, and the SAGE III forward model approximations for radiative transfer [17]. ILAS measured the *A*-band with a spectral resolution of 0.17 nm. ILAS simulation studies estimated uncertainties of 4% in pressure and 4 K in temperature at stratospheric altitudes from spectroscopic database and instrument parameter uncertainties [18].

Neither ILAS nor SAGE III have sensors able to measure in the region of the O_2 *B*-band. In fact, few studies have used the *B*-band for space-based remote sounding, although Kuze and Chance [7] discussed its potential for cloud-top height retrievals and Daniel et al. [19] showed that including the *B*-band and the weak O_2–O_2 feature at 477 nm could decrease uncertainties in *A*-band cloud parameter retrievals by as much as 50% from aircraft measurements. The Doppler shift in the rotational lines of the *B*- and γ-bands has been used to determine winds in the stratosphere [20]. To our knowledge, the only previous use of the *B*-band in solar occultation has been for tangent height corrections for the SCanning Imaging Absorption spectroMeter for Atmospheric CHartographY (SCIAMACHY) [21].

The purpose of this paper is two-fold: first, to describe and test a high-accuracy method for forward modelling *A*- and *B*-band O_2 solar occultation absorption for a low-resolution spectrometer, and, second, to

assess the use of the *B*-band for determining pressure and temperature profiles from solar occultation. With these aims in mind, the inverse method and forward model development is discussed, and the performance of the forward model is assessed using simulated data. The expected uncertainties in MAESTRO p–T profiles are determined for *A*-, *B*-, and combined *A*–*B*-band retrievals. These analyses are performed using the MAESTRO instrument line shape and instrument noise model, but their results can be generalized for any spectrometer making similar low-spectral-resolution solar occultation measurements of O_2.

2. MAESTRO O_2 measurements

A typical MAESTRO occultation measurement sequence consists of 60 spectra with tangent heights between 0 and 100 km, and approximately 20 high-Sun reference spectra. Solar occultation spectra are collected by making direct-Sun observations during satellite sunrise and sunset when the Sun–satellite vector passes through the Earth's atmosphere. Occultation spectra are heavily weighted to the tangent height where the ray passes closest to the Earth's surface and atmospheric density is at the maximum along the ray's path. The resulting measurements have high vertical resolution, as well as high signal to noise (S/N is 1000–3000 for high-Sun MAESTRO measurements). Occultation measurements are inherently self-calibrating, and the atmospheric contribution is usually represented using the transmission $T = S/S_0$ from an occultation spectrum S and a high-Sun reference spectrum S_0, or using the optical depth, $\tau = -\ln T$.

MAESTRO consists of two independent spectrometers measuring from (1) 400–545 nm (UV–Vis) and (2) 520–1010 nm (Vis–NIR). Each MAESTRO spectrometer makes spectral measurements using a concave holographic grating and a 1024-pixel photodiode array detector. The Vis–NIR spectrometer measures the O_2 bands with a slightly asymmetric Gaussian instrument line shape with a full-width-at-half-maximum (FWHM) of 2 nm, and an instantaneous instrument FOV of 1.2 km in elevation at the tangent point. McElroy et al. [1] provide a detailed description of the MAESTRO electronics and optical design.

Fig. 1 shows sample high-resolution cross-sections for the *A*- and *B*-bands, as well as simulated O_2 extinction through the atmosphere for a sample tangent height of 30 km, for a high-spectral-resolution calculation and for the MAESTRO 2-nm resolution. At this tangent altitude, the majority of the lines of the most abundant O_2 isotope have saturated, and the relatively weak branches of the less abundant isotopes become important. MAESTRO is unable to distinguish these lines, and instead measures one broad feature.

Fig. 2 shows optical depths measured on-orbit from sunset occultation ss3004 with the UV–Vis and Vis–NIR spectrometers, and the relative positions of the O_2 *A*-, *B*-, and γ-bands in MAESTRO spectra. The *A*-band is the strongest feature in these spectra, and lies in a region where other species absorb and scatter weakly. The *B*-band is also a prominent feature, though it lies in a region more affected by Chappuis-band ozone absorption, and slightly more influenced by Rayleigh and aerosol scattering than the *A*-band. The γ-band is much weaker and lies in a region of strong scattering and ozone absorption. It is generally difficult to resolve with any accuracy in MAESTRO spectra, and therefore is not considered in this analysis.

Measurements of the *A*- and *B*-band optical depths are used to derive an O_2 number density profile, which can be used to calculate the total density profile using the known-mixing ratio of O_2 (0.20947 up to approximately 85 km [22]). The total number density is then used to derive pressure using the hydrostatic equation, and a temperature profile is calculated using the ideal gas law. Although MAESTRO's low-resolution measurements prevent direct temperature inversion from relative rotational line strengths within a band, the temperature dependency of the O_2 cross-sections is still included fully within any calculations as some information on temperature is contributed by the band's low-resolution apparent shape.

3. Retrieval algorithm

The O_2 retrieval algorithm employs a global spectral fitting method, as originally developed by Carlotti [23] for infrared limb sounding, which allows for a direct inversion from spectral measurements to constituent amounts by simultaneously fitting all spectral channels at all tangent heights for one sequence of limb measurements. Following the notation of Rodgers [24], the measurement vector $\mathbf{y}$ consists of m elements $y_1, y_2, \ldots, y_m$ with measurement errors $\varepsilon_1, \varepsilon_2, \ldots, \varepsilon_m$. The state vector $\mathbf{x}$ contains elements representing the parameters to be retrieved.

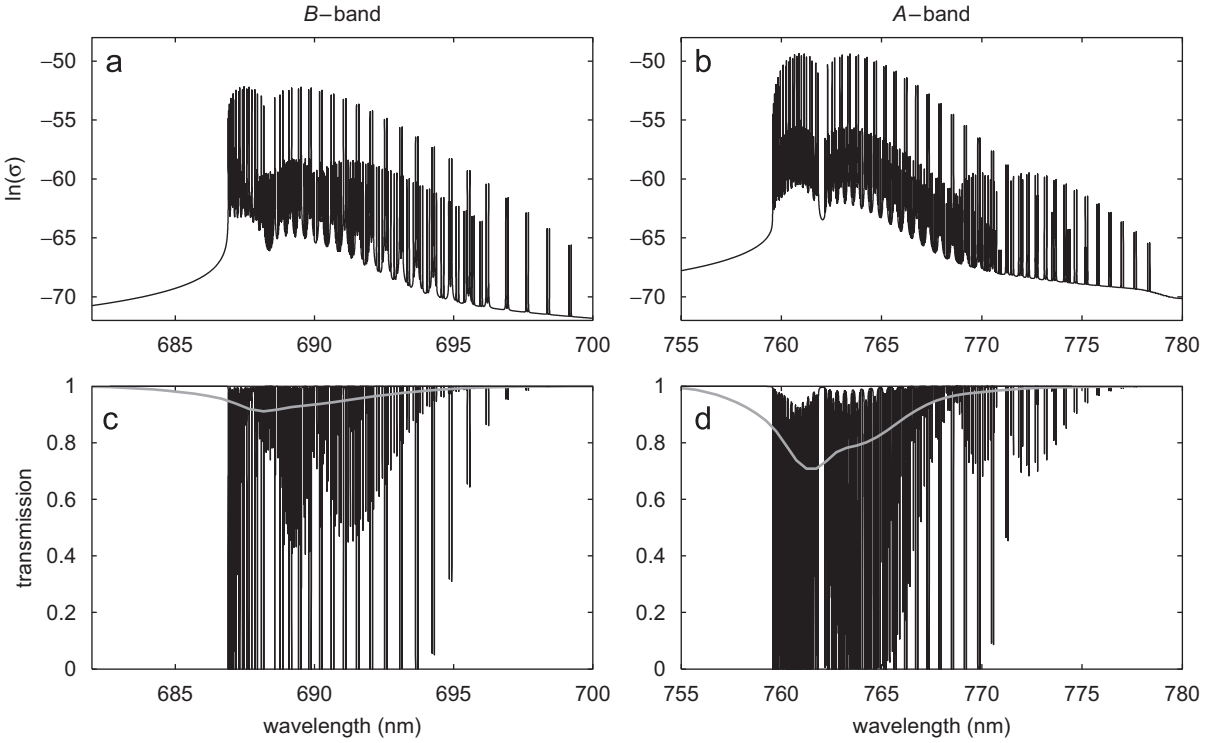

Fig. 1. (a,b) Sample O_2 *A*- and *B*-band cross-sections for a typical pressure (12 hPa) and temperature (226 K) at an altitude of 30 km and (c,d) O_2-only transmission through the atmosphere for the O_2 *A*- and *B*-bands, for a tangent height of 30 km, at high spectral resolution (black) and at the 2-nm MAESTRO spectral resolution (grey).

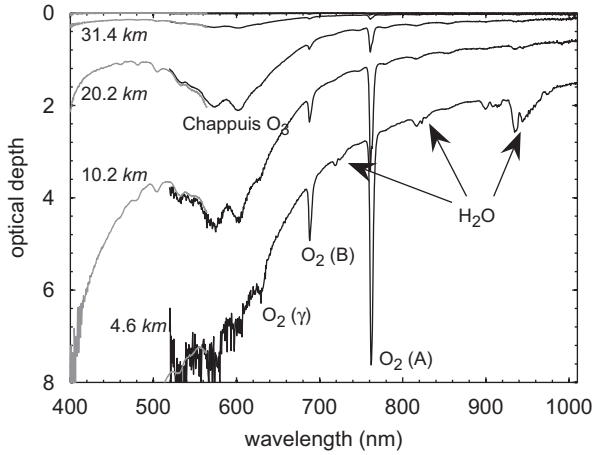

Fig. 2. MAESTRO optical depth spectra from the UV–Vis (grey) and Vis–NIR (black) spectrometers from sunset observation ss3004 (03 March 2004, 79.8°N, 80.5°W), shown for four sample tangent heights. For reference, an optical depth of 8 corresponds to a transmission of 0.03%.

A forward function **f** relates the state vector **x** and the forward function parameters **b** to the measurement vector **y**, and contains the true physics of the observation. The forward model **F(x)** is similar to the forward function, but contains any approximations to the true physics. The measurement, forward function, and forward model are related by

$$\mathbf{y} = \mathbf{f}(\mathbf{x}, \mathbf{b}) + \boldsymbol{\varepsilon} \approx \mathbf{F}(\mathbf{x}, \mathbf{b}) + \boldsymbol{\varepsilon}. \quad (1)$$

For the MAESTRO O_2 retrievals, we use an iterative constrained linearized χ^2 minimization to minimize the squared difference between the observation $\mathbf{y}$ with the covariance matrix $\mathbf{S}_\varepsilon$ and the forward model $\mathbf{F(x)}$, as expressed by

$$\chi^2_m = [\mathbf{y} - \mathbf{F(x)}]^{\mathrm{T}} \mathbf{S}_\varepsilon^{-1} [\mathbf{y} - \mathbf{F(x)}]. \tag{2}$$

In addition, the retrieval also employs a second-order Tikhonov [25] smoothing constraint, which is used to suppress oscillations in the profile resulting from measurement noise. In this case, the displacement of a retrieved value x_z is minimized relative to its two neighbours with $(x_{z-1} - 2x_z + x_{z+1})$, with terms represented by the second-derivative operator

$$\mathbf{L} = \begin{pmatrix} 1 & -2 & 1 & 0 & \cdots & 0 \\ 0 & 1 & -2 & 1 & \ddots & \vdots \\ \vdots & \ddots & \ddots & \ddots & \ddots & 0 \\ 0 & \cdots & 0 & 1 & -2 & 1 \end{pmatrix}, \tag{3}$$

and displacement described by

$$\chi^2_s = \sum (\mathbf{Lx})^2 \tag{4}$$

if $\mathbf{x}$ is defined on an evenly spaced grid.

This constrained linearized retrieval attempts to iteratively minimize $\chi^2_m + \chi^2_s$. At each iteration $i+1$, the new state is defined as

$$\mathbf{x}_{i+1} = \mathbf{x}_i + (\mathbf{K}_i^{\mathrm{T}} \mathbf{S}_\varepsilon^{-1} \mathbf{K}_i + \gamma \mathbf{H})^{-1} [\mathbf{K}_i^{\mathrm{T}} \mathbf{S}_\varepsilon^{-1} (\mathbf{y} - \mathbf{F}(\mathbf{x}_i)) - \gamma \mathbf{H} \mathbf{x}_i], \tag{5}$$

where $\mathbf{K}$ is the differential Jacobian matrix with elements $K_{pj} = \partial F_p(\mathbf{x}) / \partial x_j$, γ represents the strength of the smoothing constraint, and $\mathbf{H} = \mathbf{L}^{\mathrm{T}}\mathbf{L}$. γ is best determined optimally by a technique such as the L-curve [26]. The retrieval is iterated until convergence is reached as defined by Rodgers [24] for minimization of the state's cost function.

Furthermore, we can define a gain matrix $\mathbf{G}_y = \partial \hat{\mathbf{x}} / \partial \mathbf{y}$ to represent the sensitivity of the retrieved state to a $\Delta \mathbf{y}$ change in the measurement using

$$\mathbf{G}_y = (\mathbf{K}^{\mathrm{T}} \mathbf{S}_\varepsilon^{-1} \mathbf{K} + \gamma \mathbf{H})^{-1} \mathbf{K}^{\mathrm{T}} \mathbf{S}_\varepsilon^{-1}. \tag{6}$$

The averaging kernel matrix, $\mathbf{A}$, representing the sensitivity of a layer's retrieved state $\hat{\mathbf{x}}$ to the true state $\mathbf{x}$ at each layer is defined as

$$\mathbf{A} = \mathbf{G}_y \mathbf{K}_x = \frac{\partial \hat{\mathbf{x}}}{\partial \mathbf{x}}, \tag{7}$$

while the trace of the averaging kernel can be used to represent the independent number of degrees of freedom of the retrieval:

$$d_{\mathrm{r}} = \mathrm{tr}(\mathbf{A}). \tag{8}$$

In the case of MAESTRO, the elements of $\mathbf{y}$ represent the observed optical depth, τ_{obs}, for each pixel and observation angle, and the elements of $\mathbf{F(x)}$ represent the modelled optical depth, τ_{mod}. MAESTRO detector noise is essentially uncorrelated between pixels, and $\mathbf{S}_\varepsilon$ is constructed with the square of the estimated optical depth noise error on its diagonal, and zeros elsewhere. The retrievals are performed across each band, and to several wavelengths to the side of the band signal, so that vectors representing the background may be correctly adjusted. In the MAESTRO analyses, the A-band is fit for 55 pixels between 753 and 781 nm, and the B-band is fit for 34 pixels between 682 and 699 nm. Extending these wavelength ranges shows no improvement in retrieval performance. A combined A–B-band retrieval combines the A- and B-bands into one measurement vector $\mathbf{y}$.

The retrieved state vector **x** includes:

(1) The O_2 number densities on a 1-km altitude grid between 0 and 85 km.
(2) Aerosol terms α and β for each spectrum that represent the magnitude of the background aerosol extinction using $\tau_{aer}(\lambda) = \alpha + \beta\lambda$.
(3) A wavelength shift for each spectrum to fine-tune the pixel-wavelength calibration.

While the smoothing matrix **L** is constructed so that its non-zero terms only operate on the O_2 component of **x** in Eq. (4), the use of smoothing will cause some degree of mixing between the various terms in the solution vector. The amount of this mixing depends on the signal-to-noise level and the degree to which the O_2 vector is correlated with the other terms in the **x** vector. The O_2 *A*- and *B*-bands are very local absorbers and not correlated to any extent with the other solution vectors, and, additionally, signal to noise is high over most of the altitude range considered. Therefore, vector mixing resulting from the use of a smoothing constraint is not a serious issue.

First-guess profiles for O_2 are derived from profiles compiled at the ACE Science Operations Centre from meteorological analyses [27]. To avoid unstable matrix inversions, the natural logarithms of the number densities and scaled values of the other parameters are retrieved. The background spectral signature from ozone is determined by pre-retrieving an ozone profile using the Chappuis band between 530 and 680 nm with cross-sections from Bogumil et al. [28]. Rayleigh scattering is dependent on density and therefore inherently tied to the *p*–*T* profile. It is remodelled at each iteration according to the new density profile.

4. Forward model

The MAESTRO forward model uses a spherical-shell atmosphere consisting of a 100-m-spaced grid to calculate solar ray refraction and absorption. Multiple rays are propagated through the atmosphere to properly account for the instrument's FOV. Ignoring any azimuthal dependence (the MAESTRO slit views the entire solar disk in the azimuthal direction), the modelled signal on pixel p with wavelength λ_p, for a measurement centred about elevation angle θ_t, can be expressed as

$$S(\lambda_p, \theta_t) = R(\lambda_p) A \int_{\theta} \int_{\lambda} I(\lambda, \theta) G(\theta - \theta_t) F(\lambda - \lambda_p)\, \mathrm{d}\lambda\, \mathrm{d}\theta, \tag{9}$$

where $R(\lambda_p)$ describes the relationship of the measured detector counts to the incoming flux, A represents the slit area, $I(\lambda, \theta)$ is the monochromatic intensity incident on the instrument, $G(\theta - \theta_t)$ is the weighting of the instrument FOV about elevation angle θ_t, and $F(\lambda - \lambda_p)$ is the instrument line shape at pixel p. The slit area A is the same for an observed high-Sun spectrum S_0 and an occultation spectrum S as long as the slit is illuminated the same way for both observations (this assumption is discussed in further detail in [1]). Ignoring source terms, which is possible because of occultation geometry and MAESTRO's small FOV, the Beer–Lambert law

$$I(\lambda, \theta) = I_0(\lambda, \theta) \mathrm{e}^{-\tau(\lambda, \theta)} \tag{10}$$

can be applied in Eq. (9).

The total optical depth $\tau(\lambda, \theta)$ of one ray is the sum of the optical depths of N_c absorbers and scatterers along N_h shells:

$$\tau(\lambda, \theta) = \sum_{c=1}^{N_c} \sum_{h=1}^{N_h} \sigma_{ch}(\lambda) n_{ch} L_h(\theta). \tag{11}$$

Each shell h with molecular constituent c has a number density n_{ch}, cross-section σ_{ch}, and a path length L_h determined by the ray path. Aerosols are considered by using effective 'cross-sections' that represent the spectral characteristics of the aerosols' extinction, and an effective 'slant column' (α or β as introduced in Section 3) replaces nL, which is representative of the total slant column scatterer amount per unit area.

In order to perform the retrieval of O_2 number densities, we require an accurate forward model $\mathbf{F}(\mathbf{x})$ and an efficient and accurate calculation of **K**. As evidenced in Fig. 1, both the O_2 *A*- and *B*-bands show significant

high-resolution structure and are not broad absorbers in spectral space (unlike several other absorbers in the UV–Vis–NIR regions of the spectrum). The saturated absorption of many O_2 lines in occultation introduces a nonlinear problem, and the absorption must be modelled at high resolution in order to properly account for this saturation. This is best done with a line-by-line (LBL) calculation. The low spectral resolution of the MAESTRO instrument requires that the band be computed in its entirety for convolution with the instrument line shape.

This calculation can be very time-consuming; an LBL requires calculation of the cross-sections at each temperature and pressure, and the high-resolution spectrum must be convolved with the 2-nm instrument line shape. Even though this convolution is relatively fast if performed in Fourier space, its recalculation for 60 spectra for each column of the matrix **K** can be significant. In the following sections, two methods for improving computational efficiency are developed and assessed for accuracy in modelling the O_2 bands: (1) a fast-line-by-line (FLBL) code and (2) a modified correlated-k technique.

4.1. Fast-line-by-line

At each retrieval iteration, an LBL requires a new set of cross-sections to be calculated for the current guess of p–T combinations on the altitude grid. To improve computation speed over the LBL, an FLBL is implemented using the two-dimensional interpolation method described by Turner [29]. The FLBL allows fast cross-section computation, but radiative transfer calculations must still be performed at high spectral resolution.

The application of the FLBL involves pre-computing a cross-section table for a range of p–T combinations on a pre-defined wavenumber grid using an LBL Matlab toolbox developed at the University of Toronto [30] with O_2 parameters from HITRAN 2004 [31]. The cross-sections are stored as $\log(\sigma)$ as a function of equally spaced $\log(p/p_0)$ and T/T_0 for each wavenumber. During each iteration of a retrieval, the interpolation procedure uses a two-dimensional interpolation to compute the new $\log(\sigma)$. The pressure limits of the tables are set at 0.001 and 1060 hPa, and temperature limits are set at 180 and 320 K. On the rare occasion that a pressure or temperature exceeds these limits, the cross-section is calculated at the table limit. Both available computer memory and accuracy requirements determine the number of p–T pairs to be used in the pre-computed table. The MAESTRO FLBL table is constructed using 20 pressures and 10 temperatures. Increasing these numbers produces minimal improvements in transmission accuracy ($<0.001\%$).

The wavenumber resolution for the tables is set to $\Delta\nu = 0.005\,\mathrm{cm}^{-1}$ in order to resolve A- and B-band lines, which have typical Doppler half-widths at half-maximum on the order of $\alpha = 0.011\,\mathrm{cm}^{-1}$ for 180 K and $\alpha = 0.015\,\mathrm{cm}^{-1}$ for 320 K. The error for a MAESTRO measurement modelled using a $\Delta\nu = 0.005\,\mathrm{cm}^{-1}$ calculation versus one performed at a higher resolution of $\Delta\nu = 0.001\,\mathrm{cm}^{-1}$ is less than 0.003% in transmission at all wavelengths and tangent altitudes for both the A- and B-bands.

4.2. Correlated-k

A full development of the correlated-k approximation method for radiative transfer is given by Lacis and Oinas [32] and Goody et al. [33]. The ck-method uses the fact that the spectral transmittance for a given wavelength interval is independent of the order of the absorption coefficient, k, in that interval and can be expressed in terms of a cumulative distribution function (cdf), g. In our case, we use the cross-section σ in place of k, following the convention of UV–Vis remote sounding. This allows the transmission over a spectral interval $\lambda_{\min}$ to $\lambda_{\max}$ to be expressed as

$$T_{\bar{\lambda}}(u) = \frac{1}{\lambda_{\max} - \lambda_{\min}} \int_{\lambda_{\min}}^{\lambda_{\max}} \mathrm{e}^{-\sigma_\lambda u}\,\mathrm{d}\lambda = \int_0^1 \mathrm{e}^{-\sigma(g)u}\,\mathrm{d}g \tag{12}$$

for a slant column density $u = \int n(z)\,\mathrm{d}z$, integrated along a path of number density n. Unlike σ_λ, the function $\sigma(g)$ is relatively smooth and can be integrated using a relatively small number of points, M, using

$$T_{\bar{\lambda}}(u) \cong \sum_{j=1}^{M} \mathrm{e}^{-\sigma(g_j)u} \Delta g_j, \tag{13}$$

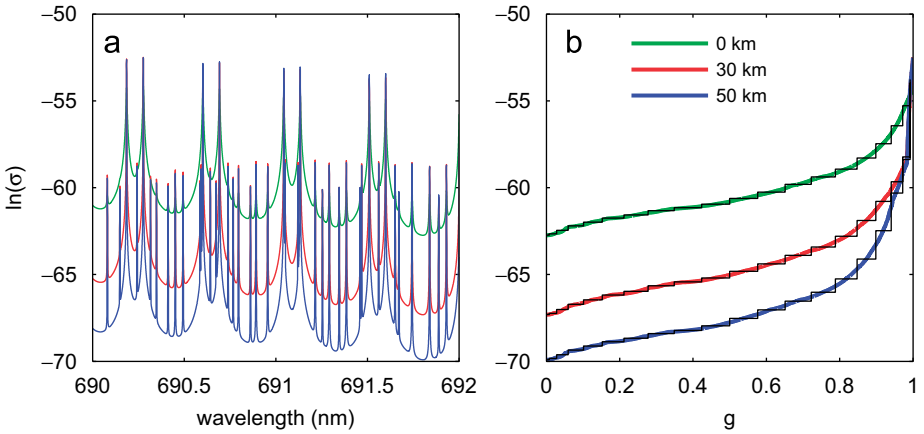

Fig. 3. (a) O_2 *B*-band cross-sections between 690 and 692 nm for a typical atmosphere at 0 km ($p = 1023$ hPa, $T = 288$ K), 30 km ($p = 12$ hPa, $T = 226$ K), and 50 km ($p = 0.8$ hPa, $T = 271$ K) and (b) their cumulative distribution functions digitized over $M = 20$ points.

thereby reducing the number of required radiative transfer calculations. Fig. 3a shows the *B*-band cross-section for the wavelength interval between 690 and 692 nm for p–T combinations typical at altitudes of 0, 30, and 50 km. Fig. 3b shows their cdf's digitized over $M = 20$ points using Gaussian quadrature weights.

As long as the relative position of a cross-section with a given wavelength is the same between cdf functions of different p–T combinations (i.e., cross-section strength is *correlated* in wavelength space), the transmission in Eq. (13) through N_h inhomogeneous paths may be calculated using

$$\sigma(g_j)u = \sum_{h=1}^{N_h} \sigma_h(g_j)u_h. \tag{14}$$

In order to apply this c*k*-method to the MAESTRO radiative transfer calculation, we must consider the more complex Eq. (9), which, after substitution with Eq. (10), contains terms for the instrument line shape and solar reference spectrum within the integral over wavelength space. Stam et al. [34] developed an extended correlated-*k* method that considered the instrument spectral response function and the solar function to simulate polarization measurements in the O_2 *A*-band. Their method is reviewed here and extended to our occultation case.

Eq. (9) gives the general expression for signal on a MAESTRO pixel. In order to simplify the expression for demonstration of the extended c*k*-method in occultation, consider only the signal S' on a pixel p that contains the convolution integral in λ space over the spectral interval from $\lambda_{\min}$ to $\lambda_{\max}$, but not the instrument functions $R(\lambda_p)$ or A, or the integration over multiple rays:

$$S'(\lambda_p) = \int_{\lambda_{\min}}^{\lambda_{\max}} I_0(\lambda)\mathrm{e}^{-\tau(\lambda)}F(\lambda - \lambda_p)\,\mathrm{d}\lambda. \tag{15}$$

If the line shape $F(\lambda - \lambda_p)$ is normalized, and a new wavelength scale is defined as $\lambda' = (\lambda - \lambda_{\min})/(\lambda_{\max} - \lambda_{\min})$ so that

$$\int_{\lambda_{\min}}^{\lambda_{\max}} F(\lambda - \lambda_p)\,\mathrm{d}\lambda = \int_0^1 F(\lambda' - \lambda'_p)\,\mathrm{d}\lambda' = 1, \tag{16}$$

the signal can now be written as

$$S'(\lambda_p) = \int_0^1 I_0(\lambda')\mathrm{e}^{-\tau(\lambda')}F(\lambda' - \lambda'_p)\,\mathrm{d}\lambda'. \tag{17}$$

In order to express S' in terms of correlated-k, we must remove I_0 and F from the integral. This is done by transforming the axis λ' to $x(\lambda')$ using

$$\mathrm{d}x = \frac{1}{C} I_0(\lambda') F(\lambda' - \lambda'_p)\,\mathrm{d}\lambda' \tag{18}$$

and

$$x(\lambda') = \frac{1}{C}\int_0^{\lambda'} I_0(y) F(y - y_p)\,\mathrm{d}y. \tag{19}$$

The constant C is calculated by setting $x(1) = 1$ and is defined by

$$C = \int_0^1 I_0(y) F(y - y_p)\,\mathrm{d}y. \tag{20}$$

After this substitution, Eq. (17) becomes

$$S'(\lambda_p) = C\int_0^1 \mathrm{e}^{-\tau(x)}\,\mathrm{d}x. \tag{21}$$

According to the ck-method, the signal S' can now be represented as

$$S'(\lambda_p) = C\sum_{j=1}^{M} \mathrm{e}^{-\tau(g_j)}\Delta g_j, \tag{22}$$

where g has been produced using cross-sections defined on the new x coordinate, rather than as a function of λ. In terms of correlated-k, and for a discrete number of solar rays N_r in the FOV, Eq. (9) is now expressed as

$$S(\lambda_p, \theta_t) = R(\lambda_p) A C \sum_{r=1}^{N_\mathrm{r}} G(\theta_r - \theta_t) \sum_{j=1}^{M} \exp\left[-\sum_{h=1}^{N_h} \sigma_h(g_j) n_h L_{hr}\right] \Delta g_j \tag{23}$$

and can also easily be generalized to include multiple absorbers [32].

Both Eqs. (9) and (23) can be differentiated with respect to O_2 density and therefore allow analytic calculation of the **K**-matrix using either the FLBL or ck-method.

4.3. Forward model approximation accuracy

An appropriate value for the number of cdf divisions, M, must be chosen for the ck calculations. Stam et al. [34] determined that $M \leqslant 30$ was sufficient for modelling their nadir-viewing O_2 simulations using a Gaussian instrument line shape with FWHM = 0.35 nm. Fig. 4 shows the absolute percent error in total optical depth, as compared to the LBL calculation, for our lower resolution measurements for various choices of M applied in Gaussian quadrature, as a function of tangent altitude. These calculations are performed using the ACE first-guess profile for the Arctic winter sunset occultation ss3004. The errors are shown at pixel wavelengths $\lambda_p = 764.5$ nm (A-band) and $\lambda_p = 687.2$ nm (B-band), where optical depth errors are at a maximum. All other pixels experience smaller errors than those illustrated in Fig. 4.

$M = 100$ is chosen for integration as larger values of M increase the number of radiative transfer calculations but provide little improvement in the correlated-k accuracy, which then becomes primarily determined by the degree of correlation between different p–T cdf functions. At these wavelengths where optical depth error is at a maximum, $M = 100$ results in total optical depth percent error of less than 1% over all altitudes. Fig. 5 shows the optical depth errors as a function of wavelength that have been introduced by the FLBL and ck approximations ($M = 100$) for sample tangent altitudes of 5 and 50 km.

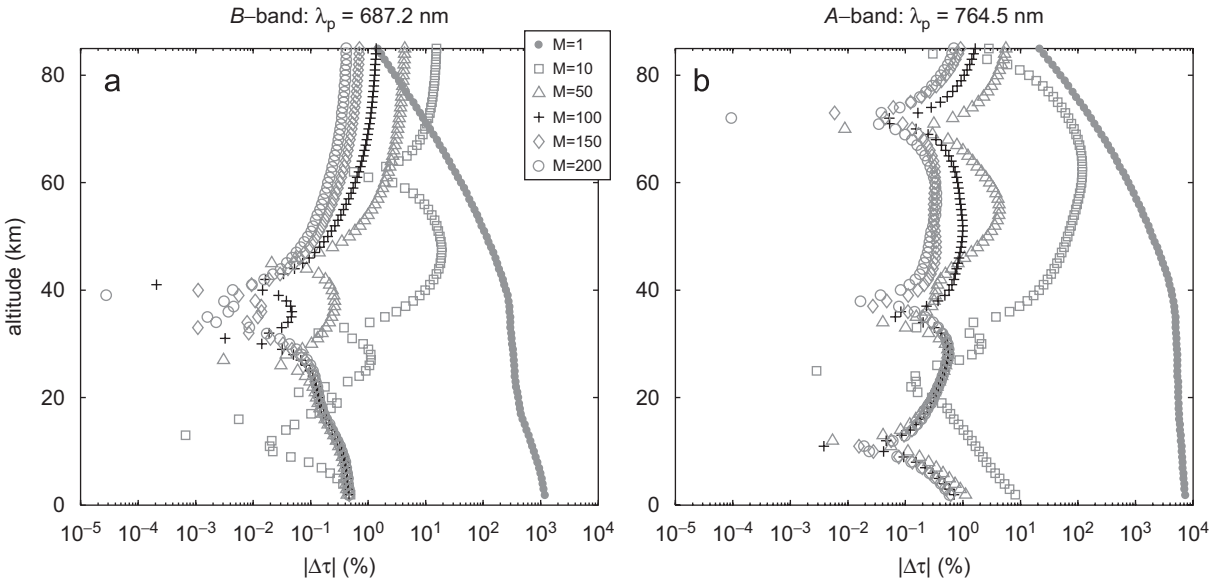

Fig. 4. Percent error in total optical depth for several values of M cdf divisions at pixels (a) $\lambda_p = 687.2$ nm and (b) $\lambda_p = 764.5$ nm as a function of tangent altitude, relative to LBL simulation.

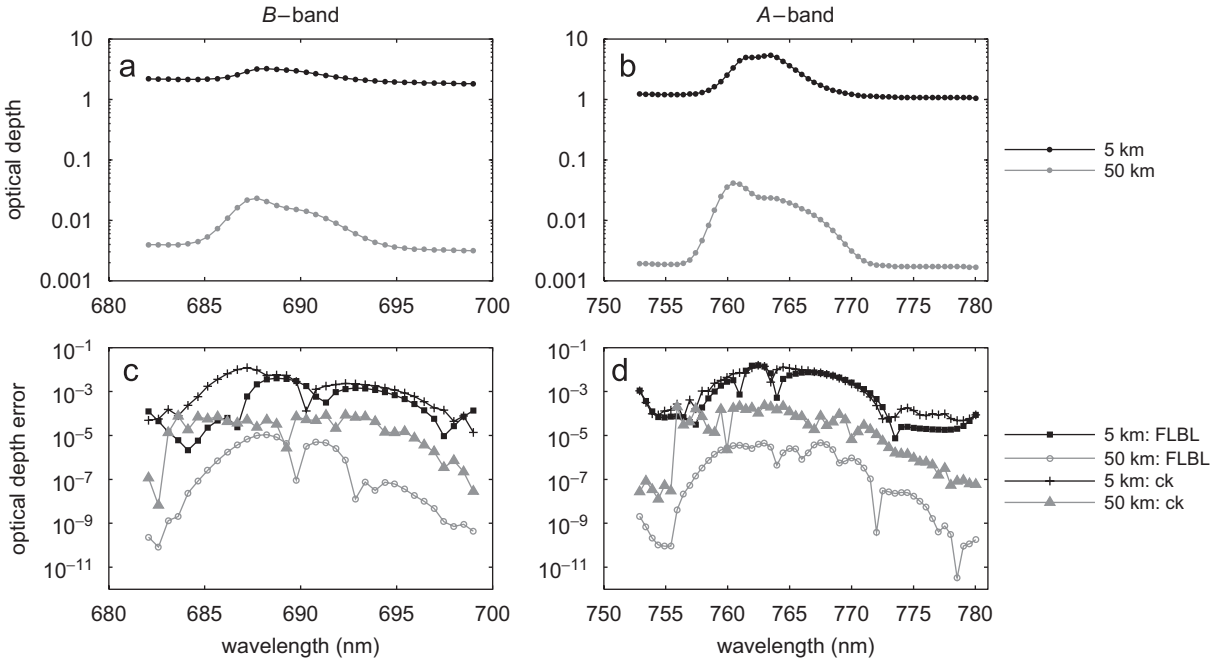

Fig. 5. (a,b) Simulated optical depth for tangent altitudes of 5 and 50 km and (c,d) optical depth errors from FLBL and correlated-k approximations relative to LBL simulation.

5. Retrieval performance

This section addresses the retrieval performance and the estimated uncertainties associated with O_2 A- and B-band retrievals from MAESTRO.

Table 1
Pressure–temperature errors and calculation times for forward modelling

F(**x**) calculation	**K** calculation	Time	Pressure error (%)	Temperature error (K)
LBL	LBL	2.8 h	n/a	n/a
FLBL	FLBL	2.3 h	<0.005	<0.05
c*k*	c*k*	8.7 min	<0.3	<1
FLBL	c*k*	10.8 min	<0.005	<0.1

Table 1 describes the errors in p–T and the calculation time for different combinations of forward modelling methods. Each calculation time given is for one typical calculation for the A- and B-bands of the forward model, **F**(**x**), and an analytic calculation of an 85-retrieval-layer Jacobian matrix, **K**, performed in Matlab on a laptop with a 1.5 GHz Centrino processor and 1 Gbyte of RAM. The given error in p–T is the limit of the error over all altitudes for a noise-free simulated retrieval (so as to not confuse errors from smoothing and noise with those from the forward model approximations) relative to a 'true' profile used to generate the simulated spectra with an LBL model.

While the FLBL provides some computational savings over the LBL, the many high-resolution radiative transfer calculations used to determine the Jacobian matrix mean that it is still too slow to be useful for the full forward model calculation. The forward model and Jacobian calculation is approximately 16 times faster using correlated-k than using the FLBL, due mainly to the elimination of high-resolution convolutions with the instrument line shape. While the ck-method is the fastest forward model to apply in the retrieval, we find a combined FLBL and ck approach, which uses the FLBL to forward model the measurement, but the ck-method for analytical calculations of the **K**-matrix best combines accuracy and efficiency. As Table 1 demonstrates, using the FLBL in combination with the ck-method can reduce temperature errors by $\sim$1 K, with a relatively small 20% increase in computation time.

5.1. Simulated measurements

Fig. 6 shows two retrievals using simulated MAESTRO spectra with realistic noise. A 'true' atmospheric profile is used to simulate measurements and artificial noise is applied that corresponds to MAESTRO's signal-to-noise ratio of 3000 at high Sun. These retrievals are performed to the surface and in this case, the US 1976 standard atmosphere is used as a first guess instead of the ACE first-guess profiles [27] to illustrate the independence of the solution on a reasonable first guess. The weight of the smoothing constraint γ is chosen independently for the A- and B-band retrievals according to the L-curve [26].

These sample retrievals are performed without aerosols. Clouds and background aerosols have nearly wavelength-independent absorption in the region of the O_2 bands and their optical depths are essentially uncorrelated to that of O_2. Their main effect is to increase the baseline optical depth of the O_2 measurement, thereby reducing the signal to noise. The addition of background aerosol levels to the simulated measurements results in little variation in the retrievals, except at the very lowest tangent heights (below 5 km) where deviations from the true profile may increase by up to 1% in pressure and 1–2 K in temperature. At times, heavy aerosol loading may occur and large optical depths will decrease retrieval sensitivity (see, for example, [17] where a dense stratospheric volcanic aerosol layer increases SAGE III pressure and temperature errors by 1.7% and 1.5 K near the layer). In practice, useful measurements are rarely available below 5–10 km due to the presence of clouds. However, measurements may be made through high-altitude cirrus clouds of modest optical depth as the physical path and multiple scattering through a thin cloud will be very small as compared to the total ray path in occultation geometry. Measurements with larger optical depth clouds can be screened for by comparing observed optical depths with those calculated using a radiative transfer model.

While a formal error analysis will be provided in Section 5.2, Fig. 6 demonstrates the relative behaviour of the A- and B-band retrievals. The large-scale errors in the retrieved profiles show the result of profile smoothing. At the locations of sharp features in the profile, the solution may have significantly more information from the smoothing constraint than from noisy measurements tangent near those altitudes, and is unable to follow precisely the gradients in the profile.

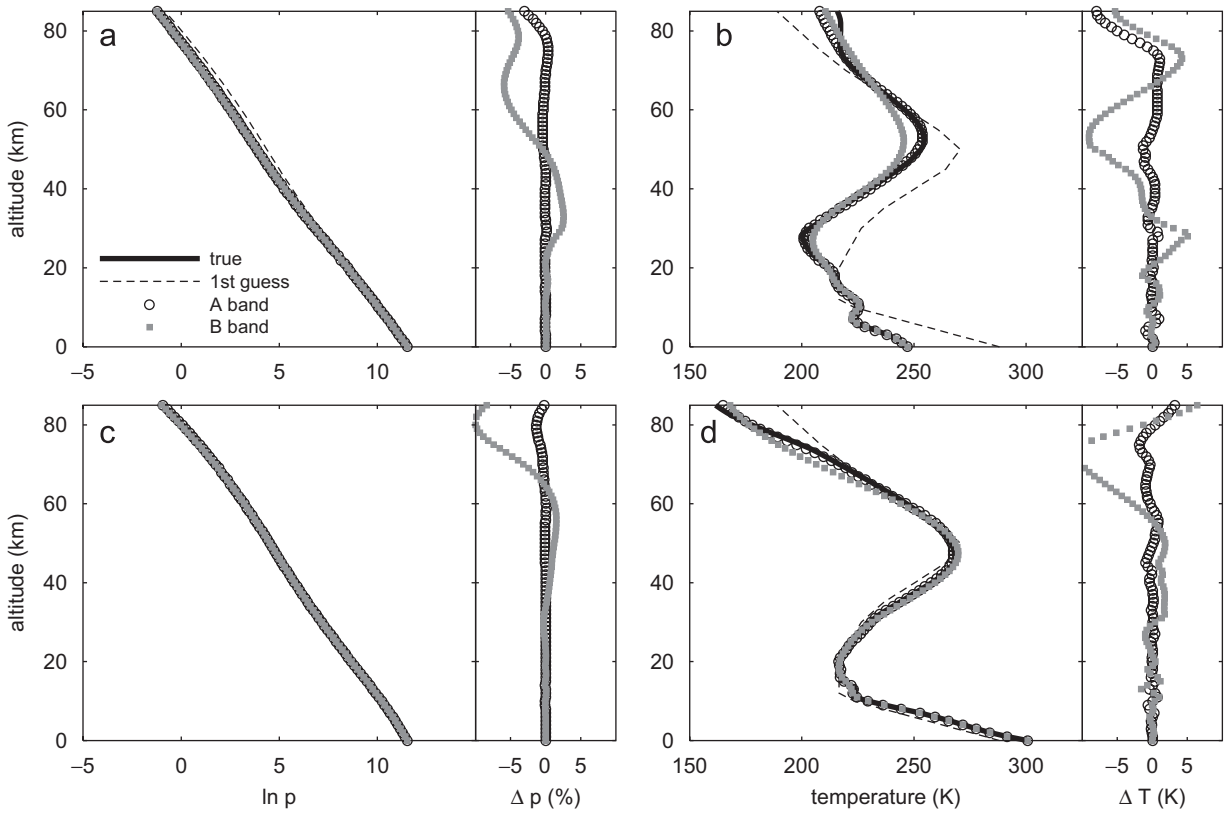

Fig. 6. Measurements of (a,b) Arctic winter occultation ss3004 (03 March 2004, 79.8°N, 80.5°W) and (c,d) mid-latitude summer occultation ss5138 (29 July 2004, 45.9°N, 46.0°W) pressure and temperature profiles, using simulated MAESTRO O_2 *A*- and *B*-band spectral observations. The differences between the measured profiles and the true (unsmoothed) profiles are shown in percent error for pressure (Δp) and in degrees K for temperature (ΔT).

5.2. Estimated uncertainties

The error analysis developed here follows the formalism of Rodgers [24]. The error, or difference between the retrieved profile $\hat{\mathbf{x}}$ and the true state $\mathbf{x}$, can be described by

(1) Smoothing error, described by covariance

$$\mathbf{S}_S = (\mathbf{A} - \mathbf{I}_n)\mathbf{S}_e(\mathbf{A} - \mathbf{I}_n)^T. \tag{24}$$

In our case, a reliable ensemble matrix, $\mathbf{S}_e$, of true states (with resolved vertical structure) about the mean is difficult to determine, at least at high altitudes where smoothing becomes significant. We instead consider the retrieved profile as an estimate of a smooth version of the true profile, rather than an estimate of the true state with a smoothing error, as recommended by Rodgers [24] for this situation.

(2) Forward model error, given by

$$\mathbf{G}_y\Delta\mathbf{f} = \mathbf{G}_y[\mathbf{f}(\mathbf{x},\mathbf{b}) - \mathbf{F}(\mathbf{x},\mathbf{b})], \tag{25}$$

which represents the error introduced by the use of the forward model $\mathbf{F}$ in Eq. (1), which may contain approximations, instead of $\mathbf{f}$, which represents the true physics.

(3) Model parameter error, described by covariance

$$\mathbf{S}_f = \mathbf{G}_y\mathbf{K}_b\mathbf{S}_b\mathbf{K}_b^T\mathbf{G}_y^T, \tag{26}$$

where $\mathbf{S}_b$ represents the covariance of model parameter uncertainties.

(4) Retrieval noise, represented by covariance

$$\mathbf{S}_m = \mathbf{G}_y \mathbf{S}_\varepsilon \mathbf{G}_y^{\mathrm{T}}. \tag{27}$$

This analysis is performed for the Arctic winter retrieval shown in Fig. 6 to illustrate a typical error analysis. In order to compare errors between A, B, and a combined A–B retrieval, where both bands are retrieved simultaneously, the γ smoothing parameter is adjusted to maintain a constant number of degrees of freedom for each retrieval (see [35], for example). We use $d_r = 24$, typical of an A–B retrieval where γ is chosen optimally. In this way, covariance between layers is similar for the three retrievals, and this discussion is limited to the errors $\varepsilon_x(i) = \sqrt{\mathbf{S}_x(i,i)}$, calculated using the diagonal elements of the error covariance matrices. Fig. 7 shows the widths (FWHM) of the sharply peaked $\ln n_{O_2}$ averaging kernels for an A–B retrieval with $d_r = 24$. The retrieval is most sensitive below 35 km, with $d_r = 15$ at these lower altitudes.

Systematic and random errors require slightly different treatment as they propagate differently from the retrieved density to the derived p–T quantities. Random errors in p–T are calculated using standard error propagation. However, a systematic error (for example, all O_2 line strengths could be too large) would likely cause all density errors to be of the same sign, and therefore all pressure errors would be of the same sign. However, as the average temperature within a layer is calculated using the ideal gas law in combination with the hydrostatic equation, its value is dependent on a ratio of the pressure at the top to that at the bottom of the layer. Systematic errors, where the pressure at the top and bottom of the layer are both likely either under- or overestimated, tend to have a cancelling effect on the uncertainty in temperature. In other words, temperature errors have little dependency on absolute pressure uncertainty and more on the gradient of the error, causing systematic errors to have minimal impact on temperature uncertainty, and allowing random errors to dominate the temperature error budget. Systematic temperature errors are plotted but should be used with caution; they may be highly variable due to their high dependency on the pressure error gradient.

5.2.1. Forward model error

In the case of forward model error, the only forward model approximations where the 'true' physics is well known are the FLBL and correlated-k approximations as opposed to the LBL 'truth'. Quantification of the forward model error is essential to assess the value of using the FLBL and correlated-k approximations. While Figs. 4 and 5 illustrate the optical depth errors introduced by these approximations ($\Delta\mathbf{f}$ in Eq. (25)), it is the forward model error that describes how these optical depth errors propagate to the p–T product.

Fig. 8 shows the error in p–T introduced by the use of the FLBL and ck-method. When the FLBL is used to forward model the O_2 radiative transfer, the resulting errors are essentially negligible ($\Delta p < 0.01\%$, $\Delta T < 0.03$ K), and demonstrate the high accuracy of the FLBL MAESTRO forward model. The ck-induced errors are quite small (generally within 1 K for temperature and 1% for pressure) for the A-band and A–B

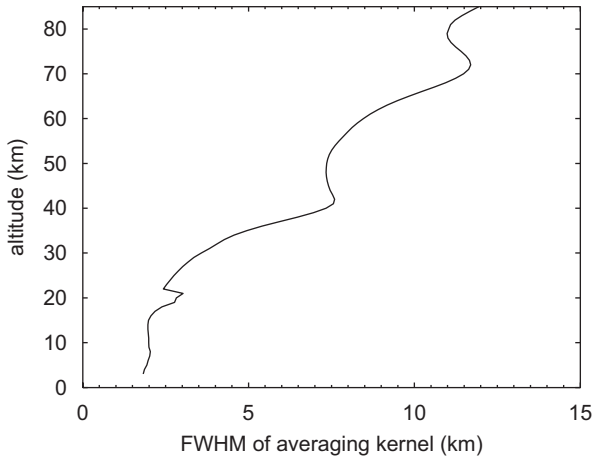

Fig. 7. FWHM of $\ln n_{O_2}$ averaging kernels for an A–B retrieval with $d_r = 24$.

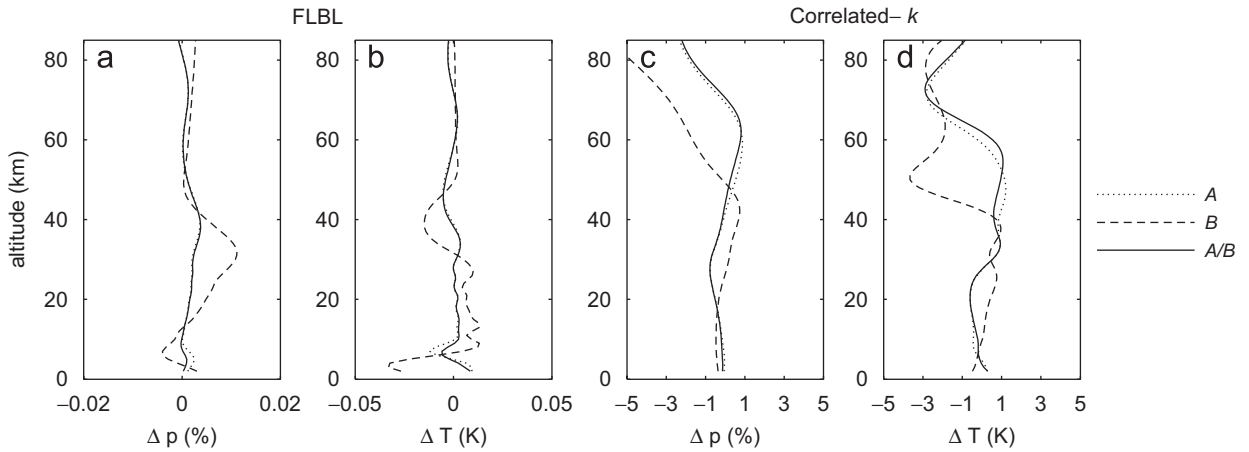

Fig. 8. Forward model errors from use of (a,b) FLBL and (c,d) correlated-k approximations for pressure (Δp) and temperature (ΔT).

retrieval up to about 60 km, and for the B-band retrieval up to about 40 km. When we desire a very fast computation, it is therefore appropriate to use the ck-method for calculating both the forward model, $\mathbf{F}(\mathbf{x})$, and the Jacobian, $\mathbf{K}$. However, as mentioned previously, using the FLBL to calculate $\mathbf{F}(\mathbf{x})$ and the ck-method to calculate $\mathbf{K}$ analytically optimizes accuracy while keeping the number of required radiative transfer calculations minimal. In this case, the forward model error is similar to that for the FLBL, as shown in Table 1, since the ck-method is used to calculate $\mathbf{G}_y$, but $\Delta\mathbf{f}$ in Eq. (25) remains the same.

5.2.2. Forward model parameter error

The main error contributions from the forward model parameters are uncertainties in O_2 spectroscopy, satellite pointing, and instrument line shape width. The errors introduced in the p–T profiles from these sources are illustrated in Fig. 9. Uncertainties in O_3 cross-sections also exist and can particularly affect A-band retrievals [36], but as the MAESTRO retrieval algorithm simultaneously retrieves aerosol offsets with O_2, uncertainties in O_3 cross-sections propagate almost entirely to uncertainties in the retrieved offset values, and as such are not considered here.

The sensitivity of the forward model to the O_2 line parameters contained in the HITRAN database ($\mathbf{K}_b$) is determined by perturbation of the line parameters by their estimated uncertainties, and recalculation of the forward model. The uncertainties for the A-band are taken from those estimated by Brown and Plymate [37], which are 2.0% in absolute line strength, 2.5% in the air and self-broadened half-widths, and 15% in the temperature dependency of the width. In this analysis, these uncertainties are considered to represent possible systematic biases in all the database lines in one band.

Uncertainties in the HITRAN 2004 B-band line parameters are not well quantified. Neither the HITRAN 2004 database nor Giver et al. [38], the experimental source of the HITRAN B-band parameters, give estimates of the absolute accuracies of most of the B-band line parameters, although Giver et al. cite a band intensity precision of 1.5% and half-width precision exceeding 2–3%, and the HITRAN database lists air-broadened half-width uncertainties of 2–5% for most major B-band lines. As a result, the A-band uncertainties are also applied here to the B-band, with the exception of the self-broadened half-width. The B-band self-broadened half-width data of Giver et al. and Barnes and Hays [39] differ by approximately 10%, a value which is used for this analysis. Newnham and Ballard [40] show a 1% agreement in B-band intensities with Giver et al. [38], suggesting that at least the line strengths of the B-band are likely to be well characterized. Estimated errors in the p–T profiles from these O_2 spectroscopic uncertainties are shown in Figs. 9a and b.

A recent study by Yang et al. [41] suggests even the spectroscopy of the A-band requires improvement. Laboratory measurements by Tran et al. [42] quantified line-mixing and collision-induced absorption in the A-band, which may eventually improve A-band modelling as these effects are not currently modelled in HITRAN.

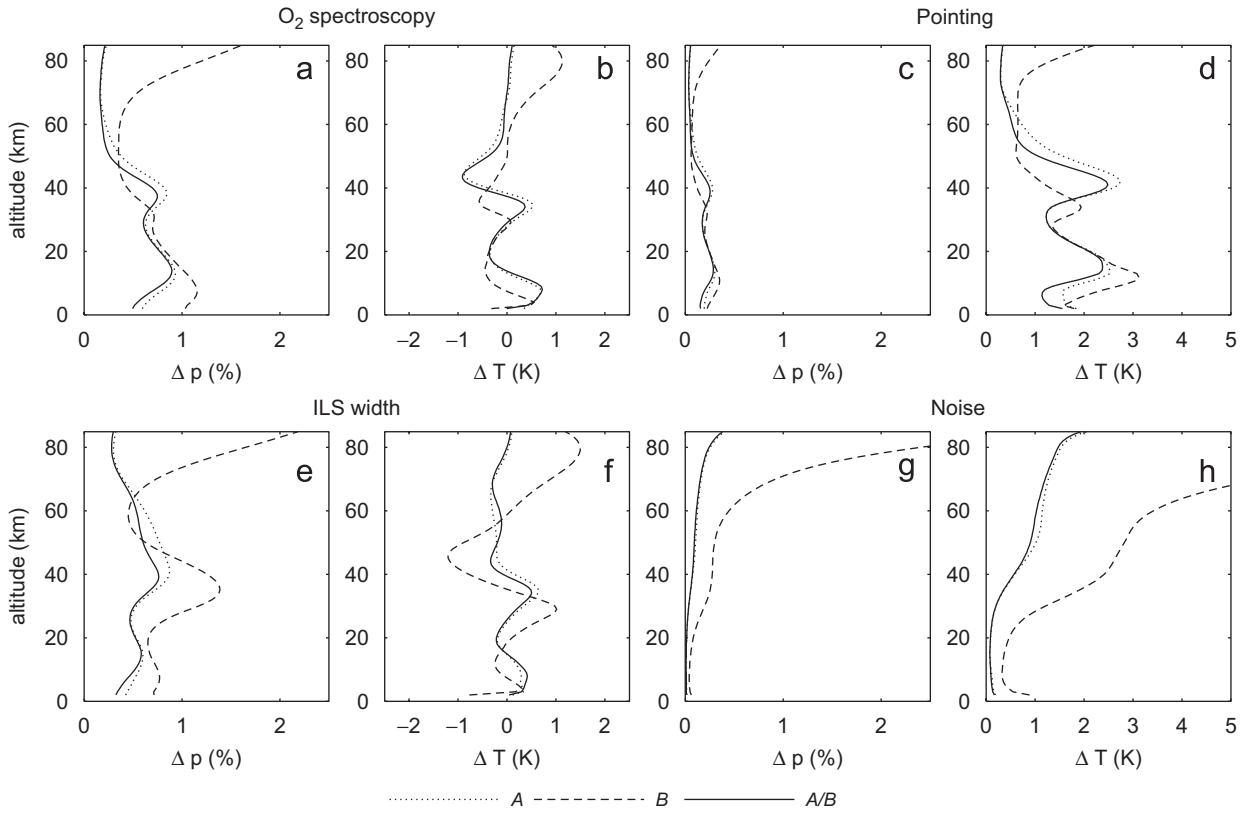

Fig. 9. Errors in pressure (Δp) and temperature (ΔT) associated with forward model parameters from (a,b) O_2 spectroscopic line database uncertainties, (c,d) a 0.002° error in pointing, (e,f) a 5% error in instrument line shape width, as well as (g,h) retrieval noise error.

Uncertainty in the instrument FOV pointing angle contributes uncertainty to the estimated ray path, and therefore the altitude registration of the observed O_2 number density. The pointing uncertainty considered here is random, although there may also be a systematic component. Figs. 9c and d show the errors expected from a 0.002° random uncertainty in the solar pointing, which corresponds roughly to a 100-m tangent altitude uncertainty from SCISAT's orbit.

There is also uncertainty associated with the width of the instrument line shape. In UV–Vis–NIR low-resolution spectrometers like MAESTRO, the width of the line shape usually varies with wavelength across the detector. Uncertainties in the width may result from only collecting line shape measurements at discrete wavelengths during pre-launch characterization and slight changes in instrument focus after launch. It may be possible to refine the line shape width by comparing modelled solar spectra and observed solar reference spectra, but there is still a remaining uncertainty defined by the availability of sharp solar features at various wavelengths and by fitting uncertainties. Figs. 9e and f show the errors in pressure and temperature associated with a 5% uncertainty in the line shape width. Errors tend to be largest in the stratosphere, where the temperature is high and wings of each band are heavily populated, so that there is high sensitivity to any perturbation affecting the width of the band.

5.2.3. *Retrieval noise*

Estimates for retrieval noise error are shown in Figs. 9g and h. These are calculated assuming a maximum S/N of 3000 for high-Sun spectra. The retrieval noise error is less than 2 K in temperature and 0.5% in pressure over all altitudes using the *A*-band, and small in the *B*-band until its rapid growth at altitudes greater than about 35 km.

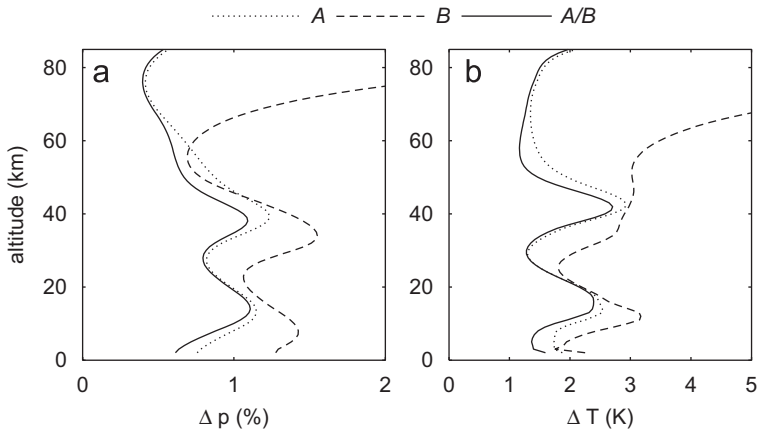

Fig. 10. Total estimated error in (a) pressure and (b) temperature for *A*, *B*, and *A–B* combined retrievals.

5.2.4. Total error

The total error estimates shown in Fig. 10 are determined by the square root of the sum of squares of the various error sources. Random and systematic errors are treated similarly, although systematic temperature errors must be treated with some caution. These errors contribute less than 0.5 K at most altitudes, but are highly dependent on the gradients in systematic pressure errors. We retrieve O_2 number density, whereas *p–T* are derived products. For this reason, and as mentioned at the beginning of Section 5, systematic and random errors propagate differently to uncertainties in derived *p–T*; systematic errors dominate the pressure error estimates, while random error contributions dominate the temperature uncertainties.

The *B*-band errors are similar to the *A*-band and combined *A–B* errors at altitudes below about 50 km. The combined retrieval is heavily weighted to the *A*-band, but its errors are always smaller as it receives some contribution from the *B*-band signal. Below 15 km and above 40 km, the combined retrieval noticeably outperforms both bands, and shows an improvement over the *A*-band retrieval of up to 0.25% in pressure and 0.5 K in temperature. This provides an improvement in our *p–T* products of roughly 25% of the MAESTRO *p–T* accuracy requirements of 1% and 2–3 K. As the addition of the *B*-band to the retrieval significantly increases computation time, accuracy requirements must be weighed against computational efficiency requirements when deciding whether to include the *B*-band for a combined retrieval.

These results also suggest that the *B*-band may be used by itself below about 50 km, although the combined retrieval produces the best results at all altitudes. The combined approach results in error estimates less than 2 K in temperature and 1% in pressure at most altitudes.

6. Summary

We have developed and assessed a method for determining pressure and temperature profiles from the MAESTRO satellite instrument's measurements of solar absorption of molecular oxygen. This was achieved through the development of forward model and retrieval algorithms using simulated MAESTRO data. To our knowledge, this work presents the first assessment of using the O_2 *B*-band for determining pressure and temperature profiles from an occultation instrument, and also includes an analysis of the *A*-band and combined *A–B* retrievals for pressure and temperature measurements as applied to MAESTRO.

The main challenge of modelling the high-spectral-resolution O_2 bands for these low-resolution retrievals was to develop a high-accuracy forward model that could model the many saturated absorption lines of O_2, but would be computationally fast enough to allow for the calculation of analytical Jacobian weighting functions for the retrieval. A correlated-*k* technique was applied to the solar occultation case that allowed the inclusion of instrument line shape information within the correlated-*k* distribution functions, thereby removing the need for time-consuming convolutions. The use of an FLBL to forward model the observation and correlated-*k* to determine the weighting functions provides a fast calculation while allowing the forward

modelling error to be essentially negligible ($\Delta p < 0.01\%$, $\Delta T < 0.03$ K at most altitudes for *A*, *B*, or *A–B* retrievals with typical smoothing).

An iterative global-fitting algorithm with a second-order smoothing constraint was developed to allow the retrieval of an O_2 density profile using either the *A*-, *B*-, or a combined *A–B*-band retrieval. The density profile is then used to derive pressure and temperature profiles through the hydrostatic equation and ideal gas law. Error analysis with simulated data showed that pressures should be able to be determined to within 1% and temperatures to within 2 K over most altitudes using the combined *A–B* retrieval. Model parameter error tends to dominate in the lower atmosphere, while measurement noise dominates at high altitudes where O_2 signal is weak.

While the *A–B* combined retrieval does provide the lowest error estimates, the *B*-band retrieval error is generally 1–1.5% in pressure and 2–3 K in temperature below about 50 km, and the *B*-band can foreseeably be used alone in a retrieval at these altitudes. The ability to retrieve using the *B*-band alone could be useful in a spectrometer whose long wavelength measurements include the *B*-band, but stop before 760 nm, or in the case where the spectrometer is better characterized in the region of the *B*-band than in that of the *A*-band. For instance, preliminary analysis of on-orbit MAESTRO O_2 data indicates that both the instrument line shape and stray light contribution are likely better known in the region of the *B*-band than at the *A*-band. In fact, MAESTRO O_2 retrievals of on-orbit data are currently using only the *B*-band below 30 km while improvements are being made to the instrument characterization model in the region of the *A*-band. Above this altitude, a combined retrieval is applied.

An assessment of the preliminary results from MAESTRO measurements of pressure and temperature using the O_2 *A*- and *B*-bands will be provided in a succeeding paper.

Acknowledgement

MAESTRO is supported by Environment Canada, the Canadian Space Agency, the Natural Sciences and Engineering Research Council, and the Canadian Foundation for Climate and Atmospheric Sciences.

References

[1] McElroy CT, Nowlan CR, Drummond JR, Bernath PF, Barton DV, Dufour DG, et al. The ACE–MAESTRO instrument on SCISAT: description, performance, and preliminary results. Appl Opt 2007;46(20):4341–56.
[2] Bernath PF, McElroy CT, Abrams MC, Boone CD, Butler M, Camy-Peyret C, et al. Atmospheric chemistry experiment (ACE): mission overview. Geophys Res Lett 2005;32:L15S01.
[3] Yamamoto G, Wark DQ. Discussion of a letter by R.A. Hanel: 'determination of cloud attitude from a satellite'. J Geophys Res 1961;66:3596.
[4] Wark DQ, Mercer DM. Absorption in the atmosphere by the oxygen "*A*" band. Appl Opt 1965;4:839–45.
[5] Mitchell RM, O'Brien DM. Error estimates for passive satellite measurement of surface pressure using absorption in the *A* band of oxygen. J Atmos Sci 1987;44:1981–90.
[6] Fisher J, Grassl H. Detection of cloud-top height from backscattered radiances within the oxygen *A* band. Part 1: theoretical study. J Appl Meteorol 1991;30:1245–59.
[7] Kuze A, Chance KV. Analysis of cloud top height and cloud coverage from satellites using the O_2 *A* and *B* bands. J Geophys Res 1994;99:14481–91.
[8] Bréon F-M, Bouffiès S. Land surface pressure estimate from measurements in the oxygen *A* absorption band. J Appl Meteorol 1996;35:69–77.
[9] Koelemeijer RBA, Stammes P, Hovenier JW, De Haan JF. A fast method for retrieval of cloud parameters using oxygen *A* band measurements from the global ozone monitoring experiment. J Geophys Res 2001;106:3475–90.
[10] Dubuisson P, Borde R, Schmechtig C, Santer R. Surface pressure estimates from satellite data in the oxygen *A*-band: applications to the MOS sensor over land. J Geophys Res 2001;106:27277–86.
[11] van Diedenhoven B, Hasekamp OP, Aben I. Surface pressure retrieval from SCIAMACHY measurements in the O_2 *A* band: validation of the measurements and sensitivity on aerosols. Atmos Chem Phys 2005;5:2109–20.
[12] Crisp D, Atlas RM, Breon F-M, Brown LR, Burrows JP, Ciais P, et al. The orbiting carbon observatory (OCO) mission. Adv Space Res 2004;34:700–9.
[13] Ortland DA, Hays PB, Skinner WR, Yee J-H. Remote sensing of mesospheric temperature and $O_2(^1\Sigma)$ band volume emission rates with the high-resolution Doppler imager. J Geophys Res 1998;103:1821–35.
[14] Wallace L, Hunten DM. Dayglow of the oxygen *A* band. J Geophys Res 1968;73:4813–33.

[15] Heller JW, Christensen AB, Yee JH, Sharp WE. Mesospheric temperature inferred from daytime observation of the O_2 atmospheric (0, 0) band system. J Geophys Res 1991;96:19499–505.
[16] Matsuzaki A, Nakamura Y, Itoh T. Rocket observation of the rotational profile of the *A*-band absorption spectrum of atmospheric oxygen molecule. Ann Geophys 1984;2:475–80.
[17] Pitts MC. Retrieval of temperature and pressure profiles for the stratospheric aerosol and gas experiment III. PhD thesis, The College of William and Mary in Virginia; 1999.
[18] Sugita T, Yokota T, Nakajima T, Nakajima H, Waragai K, Suzuki M, et al. Temperature and pressure retrievals from the O_2 *A*-band absorption measurements made by ILAS: retrieval algorithm and error analyses. In: Sasano Y, Wang J, Hayasaka T, editors. Optical remote sensing of the atmosphere and clouds II. Proceedings of the SPIE, vol. 4150; 2001. p. 94–105.
[19] Daniel JS, Solomon S, Miller HL, Langford AO, Portmann RW, Eubank CS. Retrieving cloud information from passive measurements of solar radiation absorbed by molecular oxygen and O_2–O_2. J Geophys Res 2003;108.
[20] Ortland DA, Skinner WR, Hays PB, Burrage MD, Lieberman RS, Marshall AR, et al. Measurements of stratospheric winds by the high resolution Doppler imager. J Geophys Res 1996;101:10351–63.
[21] Meyer J, Schlesier A, Rozanov A, Bovensmann H, Burrows J. Towards O_3 and NO_2 vertical profile retrieval from SCIAMACHY solar occultation measurements: first results. Adv Space Res 2004;34:744–8.
[22] Anderson GP, Chetwynd JH, Clough SA, Shettel EP, Kneizys FX. AFGL atmospheric constituent profiles (0–120 km). Technical Report, 954, Air Force Geophysics Laboratory; 1986.
[23] Carlotti M. Global-fit approach to the analysis of limb-scanning atmospheric measurements. Appl Opt 1988;27:3250–4.
[24] Rodgers CD. Inverse methods for atmospheric sounding: theory and practice. Singapore: World Scientific; 2000.
[25] Tikhonov AN. Solution of incorrectly formulated problems and the regularization method. Dokl Akad Nauk SSSR 1963;151:501–4.
[26] Hansen PC. Analysis of discrete ill-posed problems by means of the *L*-curve. SIAM Rev 1992;34:561–80.
[27] Boone CD, Nassar R, Walker KA, Rochon Y, McLeod SD, Rinsland CP, et al. Retrievals for the atmospheric chemistry experiment Fourier-transform spectrometer. Appl Opt 2005;44:7218–31.
[28] Bogumil K, Orphal J, Homann T, Voigt S, Spietz P, Fleischmann OC, et al. Measurements of molecular absorption spectra with the SCIAMACHY pre-flight model: instrument characterization and reference data for atmospheric remote-sensing in the 230–2380 nm region. J Photochem Photobiol A: Chem 2003;157:167–84.
[29] Turner DS. Absorption coefficient estimation using a two-dimensional interpolation procedure. JQSRT 1995;53:633–7.
[30] Quine BM, Drummond JR. GENSPECT: a line-by-line code with selectable interpolation error tolerance. JQSRT 2002;74:147–65.
[31] Rothman LS, Jacquemart D, Barbe A, Chris Benner D, Birk M, Brown LR, et al. The HITRAN 2004 molecular spectroscopic database. JQSRT 2005;96:139–204.
[32] Lacis AA, Oinas V. A description of the correlated *k* distribution method for modeling nongray gaseous absorption, thermal emission, and multiple scattering in vertically inhomogeneous atmospheres. J Geophys Res 1991;96:9027–63.
[33] Goody R, West R, Chen L, Crisp D. The correlated-*k* method for radiation calculations in nonhomogeneous atmospheres. JQSRT 1989;42:539–50.
[34] Stam DM, De Haan JF, Hovenier JW, Stammes P. A fast method for simulating observations of polarized light emerging from the atmosphere applied to the oxygen-*A* band. JQSRT 2000;64:131–49.
[35] Steck T. Methods for determining regularization for atmospheric retrieval problems. Appl Opt 2002;41:1788–97.
[36] Pitts MC, Thomason LW, Zawodny JM, Wenny BN, Livingston JM, Russell PB, et al. Ozone observations by the gas and aerosol measurement sensor during SOLVE II. Atmos Chem Phys 2006;6:2695–709.
[37] Brown LR, Plymate C. Experimental line parameters of the oxygen *A* band at 760 nm. J Mol Spectrosc 2000;199:166–79.
[38] Giver LP, Boese RW, Miller JH. Intensity measurements, self-broadening coefficients, and rotational intensity distribution for lines of the oxygen *B* band at 6880 Å. JQSRT 1974;14:793–802.
[39] Barnes JE, Hays PB. Pressure shifts and pressure broadening of the *B* and γ bands of oxygen. J Mol Spectrosc 2002;216:98–104.
[40] Newnham DA, Ballard J. Visible absorption cross sections and integrated absorption intensities of molecular oxygen (O_2 and O_4). J Geophys Res 1998;103:28801–16.
[41] Yang Z, Wennberg PO, Cageao RP, Pongetti TJ, Toon GC, Sander SP. Ground-based photon path measurements from solar absorption spectra of the O_2 *A*-band. JQSRT 2005;90:309–21.
[42] Tran H, Boulet C, Hartmann J-M. Line-mixing and collision-induced absorption by oxygen in the *A* band. Laboratory measurements, model, and tools for atmospheric spectra computations. J Geophys Res 2006;111:D15210.